INTERNATIONAL JOURNAL FOR NUMERICAL METHODS IN FLUIDS
Int. J. Numer. Meth. Fluids 2007; **55**:917–943
Published online 4 October 2007 in Wiley InterScience (www.interscience.wiley.com). DOI: 10.1002/fld.1469

High-order ENO and WENO schemes for unstructured grids

W. R. Wolf[1] and J. L. F. Azevedo[2,*,†]

[1]*Instituto Tecnológico de Aeronáutica, CTA/ITA, São José dos Campos, São Paulo 12228-900, Brazil*
[2]*Instituto de Aeronáutica e Espaço, CTA/IAE, São José dos Campos, São Paulo 12228-903, Brazil*

SUMMARY

This work describes the implementation and analysis of high-order accurate schemes applied to high-speed flows on unstructured grids. The class of essentially non-oscillatory schemes (ENO), that includes weighted ENO schemes (WENO), is discussed in the paper with regard to the implementation of third- and fourth-order accurate methods. The entire reconstruction process of ENO and WENO schemes is described with emphasis on the stencil selection algorithms. The stencils can be composed by control volumes with any number of edges, e.g. triangles, quadrilaterals and hybrid meshes. In the paper, ENO and WENO schemes are implemented for the solution of the dimensionless, 2-D Euler equations in a cell centred finite volume context. High-order flux integration is achieved using Gaussian quadratures. An approximate Riemann solver is used to evaluate the fluxes on the interfaces of the control volumes and a TVD Runge–Kutta scheme provides the time integration of the equations. Such a coupling of all these numerical tools, together with the high-order interpolation of primitive variables provided by ENO and WENO schemes, leads to the desired order of accuracy expected in the solutions. An adaptive mesh refinement technique provides better resolution in regions with strong flowfield gradients. Results for high-speed flow simulations are presented with the objective of assessing the implemented capability.

Received 25 July 2006; Revised 27 January 2007; Accepted 30 January 2007

KEY WORDS: ENO schemes; WENO schemes; unstructured grids; aerodynamics; compressible flow

1. INTRODUCTION

In the present paper, the authors continue the effort of implementing high-order accurate schemes for the solution of hyperbolic conservation laws in an unstructured grid context [1]. The motivation

*Correspondence to: J. L. F. Azevedo, Instituto de Aeronáutica e Espaço, CTA/IAE/ASA-L, São José dos Campos, São Paulo 12228-903, Brazil.
†E-mail: azevedo@iae.cta.br, joaoluiz.azevedo@gmail.com

Contract/grant sponsor: Fundação de Amparo à Pesquisa do Estado de São Paulo, FAPESP; contract/grant number: 03/10047-2
Contract/grant sponsor: Conselho Nacional de Desenvolvimento Científico e Tecnológico, CNPq; contract/grant number: 501200/2003-7

for the work is the need for accurate simulations of high Mach number aerodynamic flows with strong discontinuities. In recent years, several efforts have been made by the Computational Fluid Dynamics (CFD) group of Instituto de Aeronáutica e Espaço (IAE) [2–4] for the development of computational tools which are able of accurately capturing discontinuities such as the shock waves appearing in the aerodynamic flows of interest. Some upwind schemes such as the van Leer flux vector splitting scheme [5], the Liou AUSM$^+$ flux vector splitting scheme [6] and the Roe flux difference splitting scheme [7] have been implemented and tested for second-order accuracy considering a TVD–MUSCL reconstruction [8]. However, Reference [4] shows that nominally second-order schemes presented results with an order of accuracy smaller than the expected one in the solutions for unstructured grids. Aside from this fact, it is well known that TVD schemes have their order of accuracy reduced to first order in the presence of shocks due to the effect of limiters [9].

Actually, this last observation initiated the development and implementation of essentially non-oscillatory (ENO) schemes, introduced by Harten *et al.* [10], in which oscillations up to the order of the truncation error are allowed to overcome the drawbacks and limitations of TVD schemes. Subsequent on the development of ENO schemes, the weighted ENO (WENO) schemes were introduced by Liu *et al.* [11] with the purpose of presenting better convergence rate for stationary cases, better smoothing for the flux vectors and better accuracy using the same stencils as the ENO schemes.

In this work, the ENO schemes and the WENO schemes are implemented in a cell centred finite volume context for unstructured meshes. The two-dimensional Euler equations are considered to represent the flows of interest. The ENO and WENO schemes have been developed with the purpose of accurately capturing discontinuities appearing in problems governed by hyperbolic conservation laws. In the high-speed flows of interest in the present paper, these discontinuities are mainly represented by shock waves and contact discontinuities. The entire reconstruction process of ENO and WENO schemes is described in detail for quadratic and cubic polynomials and, hence, for third- and fourth-order accurate numerical methods. The extension to arbitrary orders of spatial accuracy is straightforward from the formulation presented in the paper. For the ENO schemes, interpolation polynomials of one order less than the order of accuracy expected in the solution are computed and these polynomials are used to reconstruct a good approximation to the values of the flow variables within the cells. These polynomials interpolate primitive variable values in Gauss quadrature points using stencils determined by a von Neumann neighbourhood [12]. The control volume moments and the mean values of primitive variables in the cells are used to compute the polynomial coefficients and, hence, one can compute the oscillation indicators for the polynomials and select the smoothest among them.

While the ENO schemes use the smoothest polynomial, the WENO schemes use all ENO computed polynomials for the stencils and, therefore, they construct only one polynomial. Non-negative weights, which must add up to one, are computed for every ENO polynomial through oscillation indicators and the WENO polynomial is constructed by the sum of all the ENO polynomials multiplied by the respective weights [11, 13]. The weights attributed to the polynomials can be of the order of accuracy desired in the solution if these polynomials are in the discontinuous regions of the mesh or they can be of order one if the polynomials are in the smooth regions of the flow.

This paper is organized as follows. In Section 2, the authors recall the necessary theoretical formulation concerning the governing equations, the flux computation across the interfaces of the cells, and the time evolution of the numerical scheme. Section 3 is concerned with the implementation of ENO and WENO schemes with considerations to the basic formulation, selection

DOI: 10.1002/fld

of the oscillation indicator, reconstruction of third-order accurate schemes, and reconstruction of fourth-order accurate schemes. Particular attention is paid to the stencil selection algorithms. In Section 4, one can see a brief description of the adaptive mesh refinement technique used in the computations. In Section 5, some numerical results are presented and, finally, in Section 6, several general discussions appear in the conclusion of the paper. The results presented in Section 5 include some well documented numerical test cases such as: the Ringleb flow; the flow in a channel with a forward-facing step; the flow in a typical hypersonic inlet; and the flow over a 2-D blunt body.

2. THEORETICAL FORMULATION

2.1. Governing equations

In the present work, the 2-D Euler equations are solved in their integral form as

$$\frac{\partial}{\partial t}\int_V Q\,\mathrm{d}V + \int_V (\nabla\cdot\mathbf{P})\,\mathrm{d}V = 0 \tag{1}$$

where $\mathbf{P} = E\hat{\imath} + F\hat{\jmath}$. The application of the divergence theorem to Equation (1) yields

$$\frac{\partial}{\partial t}\int_V Q\,\mathrm{d}V + \int_S (\mathbf{P}\cdot\mathbf{n})\,\mathrm{d}S = 0 \tag{2}$$

where V represents the control volume, S represents the surface of the control volume and $\mathbf{n}$ is the unit normal vector to the surface, S, positive outward. The vector of conserved variables, Q, and the convective flux vectors, E and F, are given by

$$Q = \begin{Bmatrix} \rho \\ \rho u \\ \rho v \\ e \end{Bmatrix}, \quad E = \begin{Bmatrix} \rho u \\ \rho u^2 + p \\ \rho uv \\ (e+p)u \end{Bmatrix}, \quad F = \begin{Bmatrix} \rho v \\ \rho uv \\ \rho v^2 + p \\ (e+p)v \end{Bmatrix} \tag{3}$$

In the above equations, ρ represents the density, p is the pressure, u and v represent the Cartesian components of the velocity, and e is the total energy per unit of volume. The system is closed by the equation of state for a perfect gas

$$p = (\gamma - 1)[e - \tfrac{1}{2}\rho(u^2 + v^2)] \tag{4}$$

where the ratio of specific heats, γ, was chosen as 1.4 for all computations in this work.

Equation (2), discretized in a cell centred finite volume context, can be rewritten for the ith control volume as

$$\frac{\partial Q_i}{\partial t} = -\frac{1}{V_i}\int_{S_i} (\mathbf{P}\cdot\mathbf{n})\,\mathrm{d}S \tag{5}$$

where Q_i is the mean value of Q at time t over the ith control volume, V_i.

DOI: 10.1002/fld

2.2. Numerical flux evaluation

The spatial discretization is concerned with finding a discrete approximation to the integral in the right-hand side of Equation (5). In the present section, this discretization is discussed with respect to the formulation of the numerical flux computation. The subject of obtaining interface values for the flow properties is deferred to a latter section. The control volumes considered in this work are triangles and quadrilaterals and their boundaries can be decomposed into a finite number of line segments, Γ_j. One should observe that the control volumes could be composed by any type of polygon, because the really important aspect is that their bounding contours could be decomposed into a finite number of line segments. Hence, it is possible to write

$$S_i = \bigcup \Gamma_j \tag{6}$$

Thus, the boundary integral from Equation (5) can be decomposed into

$$\int_{S_i} (\mathbf{P} \cdot \mathbf{n}) \, \mathrm{d}S = \sum_j \int_{\Gamma_j} (\mathbf{P} \cdot \mathbf{n}) \, \mathrm{d}S \tag{7}$$

and, as $\mathbf{n}$ is constant on each line segment, Γ_j, the right side of Equation (7) is discretized using N-point Gaussian integration formulae with degree $2N-1$ and order of accuracy $2N$. Using such integration formulae, one obtains the following approximation:

$$\int_{S_i} (\mathbf{P} \cdot \mathbf{n}) \, \mathrm{d}S \approx \sum_j |\Gamma_j| \sum_{\ell=1}^{N} w_\ell \mathbf{P}(Q(G_\ell), t) \cdot \mathbf{n} \tag{8}$$

where G_ℓ and w_ℓ are, respectively, the Gaussian points and the weights on the Γ_j line segment.

For the third- and fourth-order schemes, two Gaussian points are necessary along each line segment. Given the coordinates of the end points, z_1 and z_2, one can obtain the Gaussian points as

$$G_1 = \frac{\sqrt{3}+1}{2\sqrt{3}} z_1 + \left(1 - \frac{\sqrt{3}+1}{2\sqrt{3}}\right) z_2 \quad \text{and} \quad G_2 = \frac{\sqrt{3}+1}{2\sqrt{3}} z_2 + \left(1 - \frac{\sqrt{3}+1}{2\sqrt{3}}\right) z_1 \tag{9}$$

and the respective weights, w_1 and w_2, are chosen as $w_1 = w_2 = \frac{1}{2}$.

Using the method described above, one can compute values of $\bar{Q}_i$ in some instant, t, and then, from these mean values, one can reconstruct polynomials that represent the primitive variables ρ, u, v and p. Finally, it is possible to compute values of the conserved variables in the Gaussian points. Due to the discontinuity of the reconstructed values of the conserved variables across the cell boundaries, one must use a numerical flux function to approximate these flux values along such boundaries. In the present work, the authors have used the Roe flux difference splitting method [7] to compute such approximations. Hence, the flux evaluation in the right-hand side of Equation (8) is computed as

$$\begin{aligned} \mathbf{P}(Q_j(G_\ell), t) \cdot \mathbf{n} &\approx \mathscr{P}(Q_i(G_\ell), Q_{ng}(G_\ell), t; \mathbf{n}) \\ &= \tfrac{1}{2} [\mathbf{P}(Q_i(G_\ell)) + \mathbf{P}(Q_{ng}(G_\ell))] \cdot \mathbf{n} \\ &\quad - \tfrac{1}{2} |A(Q_i(G_\ell), Q_{ng}(G_\ell), t; \mathbf{n})| [Q_{ng}(G_\ell) - Q_i(G_\ell)] \end{aligned} \tag{10}$$

DOI: 10.1002/fld

In Equation (10), the $|A|$ matrix is a positive semidefinite matrix formed from the flux Jacobian matrix in the sense defined by Roe [7]. In the same equation, $Q_i(G_\ell)$ is the vector of conserved variables computed at the quadrature point, G_ℓ, using the polynomial reconstruction associated with the ith control volume. Similarly, $Q_{ng}(G_\ell)$ is the vector of conserved variables computed at the same quadrature point, G_ℓ, but using the polynomial reconstruction associated with the ngth control volume. Here, it is being assumed that 'ng' represents the neighbour of the ith control volume, which shares the Γ_j line segment with the ith cell.

2.3. Temporal discretization

The temporal discretization is concerned with solving a system of ordinary differential equations in time. Hence, an ODE problem can be written as

$$\frac{\mathrm{d}Q_i}{\mathrm{d}t} = -\frac{1}{V_i} C(Q_i) \tag{11}$$

In the present work, a third-order fully explicit TVD Runge–Kutta scheme is used to advance the solution of the governing equations in time for the spatially third- and fourth-order schemes. It can be written as

$$\begin{aligned}
Q_i^{(0)} &= Q_i^n \\
Q_i^{(1)} &= Q_i^{(0)} - \alpha_1 \frac{\Delta t_i}{V_i} C(Q_i^{(0)}) \\
Q_i^{(2)} &= \alpha_2 Q_i^{(0)} + \alpha_3 Q_i^{(1)} - \alpha_3 \frac{\Delta t_i}{V_i} C(Q_i^{(1)}) \\
Q_i^{(3)} &= \alpha_4 Q_i^{(0)} + \alpha_5 Q_i^{(2)} - \alpha_5 \frac{\Delta t_i}{V_i} C(Q_i^{(2)}) \\
Q_i^{n+1} &= Q_i^{(3)}
\end{aligned} \tag{12}$$

where the α coefficients are $\alpha_1 = 1$, $\alpha_2 = \frac{3}{4}$, $\alpha_3 = \frac{1}{4}$, $\alpha_4 = \frac{1}{3}$, $\alpha_5 = \frac{2}{3}$, as suggested in Reference [14].

3. ENO AND WENO RECONSTRUCTIONS

3.1. General considerations

The reconstruction procedure for the ENO schemes is based on the approximation of mean values of the primitive variables for each cell in the mesh by polynomials of one order less than the expected spatial order of accuracy. For the construction of polynomials of ηth order, one must use $N(\eta)$ cells, where $N(\eta) = (\eta+1)(\eta+2)/2$. The first step in obtaining the polynomial reconstruction for each cell is to define the possible set of cells, called a stencil, that will be used. In a finite volume cell centred scheme, the stencils can be selected in a von Neumann neighbourhood for a linear polynomial reconstruction (second-order accuracy). This approach can be extended to higher orders through the use of von Neumann neighbourhoods of the primary neighbours already

DOI: 10.1002/fld

selected for the linear reconstruction. In the present work, the cells are triangles or quadrilaterals and the $p(x, y)$ polynomials can be calculated as

$$p(x, y) = \sum_{|\beta| \leqslant \eta} r_{\beta_1 \beta_2} (x - x_c)^{\beta_1} (y - y_c)^{\beta_2} \tag{13}$$

Here, $|\beta| = \beta_1 + \beta_2$, with $\beta_i \in \{0, 1, 2, \ldots\}$, x_c and y_c are the Cartesian coordinates of the barycentre of the control volume for which the reconstruction is being performed, and $r_{\beta_1 \beta_2}$ are unknown coefficients which are some approximations to the derivatives of the primitive variables.

By imposing that the integration of $p(x, y)$ along each cell of the stencil returns the mean value for the corresponding primitive variable in that cell, one can write a linear system, $[R]\{r\} = \{\overline{u}\}$, of $N(\eta)$ equations for the $N(\eta)$ unknowns, $r_{\beta_1 \beta_2}$. Here, $[R]$ is the matrix of control volume moments, as in Gooch [15], computed using the scaling technique proposed by Friedrich [13] to circumvent a poorly conditioned matrix. Moreover, $\{r\}$ is the vector of unknown coefficients that must be found and $\{\overline{u}\}$ is the vector composed by the mean values for each primitive variable. The stencil is considered admissible if the $[R]$ matrix is invertible. There are other approaches for the calculation of the polynomials, as the one proposed by Abgrall [16], which uses interpolation through barycentric coordinates, or the one proposed by Hu and Shu [17], which is based in reconstructing high-order polynomials using only linear polynomials. These alternate approaches, however, are beyond the scope of the present paper.

The control volume moments that form the $[R]$ matrix are defined as

$$\overline{x^{\varphi} y^{\zeta}} \equiv \frac{1}{V_i} \int_{V_i} (x - x_c)^{\varphi} (y - y_c)^{\zeta} \, \mathrm{d}V \tag{14}$$

and they are evaluated using Gaussian quadrature formulae following the same procedure as the one used in the flux computations. To avoid computing moments of each control volume for all the stencils, one can replace the terms $(x - x_c)$ and $(y - y_c)$ by $(x - x_{cj}) + (x_{cj} - x_c)$ and $(y - y_{cj}) + (y_{cj} - y_c)$, respectively [13, 15]. The new terms appearing in the equations are simply the split between the distances of the centroids of the V_j and V_i control volumes plus the initial terms evaluated using the centroids of the V_j volume instead of the centroids of the V_i volume. Finally, the control volume moments are calculated, saving computational cost and memory storage, by the following general form:

$$\begin{aligned} \overline{x^{\varphi} y^{\zeta}}_{ij} &\equiv \frac{1}{V_i} \int_{V_i} [(x - x_{cj}) + (x_{cj} - x_c)]^{\varphi} \left[(y - y_{cj}) + (y_{cj} - y_c)\right]^{\zeta} \mathrm{d}V \\ &= \sum_{\chi=0}^{\zeta} \sum_{\xi=0}^{\varphi} \binom{\zeta}{\chi} \binom{\varphi}{\xi} (x - x_{cj})^{\xi} (y - y_{cj})^{\chi} \overline{x^{\varphi - \xi} y^{\zeta - \chi}} \end{aligned} \tag{15}$$

After the polynomial reconstructions are performed for each cell, the next step is to verify which polynomial is the least oscillatory to use in the ENO scheme. The level of oscillation is computed using some indicator that assesses the smoothness of $p(x, y)$. Taking into consideration the results presented in the literature [1, 13], the oscillation indicator used in the present work is the one proposed by Jiang and Shu [18]. The formulation for this oscillation indicator can be

DOI: 10.1002/fld

expressed as

$$\mathrm{OI}_{\mathrm{JS}}(p(x,y)) = \left[\sum_{1 \leqslant |\beta| \leqslant \eta} \int_{V_i} h^{|\beta|-1} \left(\frac{\partial^{|\beta|} p(x,y)}{\partial x^{\beta 1} \partial y^{\beta 2}} \right)^2 \mathrm{d}x\, \mathrm{d}y \right]^{1/2} \tag{16}$$

where h is the mesh size, considered in the present computations as the diameter of the control volume inscribed circle.

Differently from the ENO schemes, the WENO schemes use all the calculated polynomials. These polynomials are added together through the use of weights which are computed for each one of the polynomials as inversely proportional to its respective oscillation indicator. The main idea in the WENO reconstruction is to attribute the computed weights for each polynomial with the aim of reconstructing a new polynomial as $p(x,y) = \sum_{k=1}^{m} \omega_k p_k(x,y)$. The weights are of order one in the smooth regions of the flow and are of the order of the desired accuracy in the solution in the regions with discontinuities. The weights can be computed as

$$\omega_k = \frac{[\varepsilon + \mathrm{OI}(p_k(x,y))]^{-\theta}}{\sum_{k'=1}^{m} [\varepsilon + \mathrm{OI}(p_{k'}(x,y))]^{-\theta}} \tag{17}$$

where ε is a small real number used to avoid division by zero and θ is a positive integer. The WENO schemes have the property of being very smooth and stable in smooth regions of the flow, but this property is lost if θ is chosen too large. In that case, the scheme tends to behave like the ENO schemes. In the present work, the θ term is chosen as $\theta = 2$, because this yielded the best convergence rates in previous computations by the authors [1].

3.2. Third-order implementation

For the implementation of the third-order accurate schemes one must use six cells for the polynomial reconstructions. Five unknown coefficients are computed for each polynomial through the solution of a 5-equation linear system. The linear system matrix is composed by the control volume moments, and the primitive variables of the cells considered in the stencil make up the forcing term. The algorithm implemented is based on the ideas proposed by Abgrall [16]. The first step consists in finding the stencil that presents the smoothest polynomial among the possible stencils for a linear reconstruction using only the primary neighbours of the main control volume [1]. The main control volume is labelled 'MAIN' in all pertinent figures throughout the paper. The algorithm uses this concept for both the ENO and WENO schemes for meshes composed by triangles and quadrilaterals. After the smoothest three-cell stencil is chosen, one can start the procedure for the third-order accuracy reconstruction. If the control volume is a triangle, one has a maximum of four secondary neighbours for the reconstruction and, therefore, four possibilities of stencils for the selection. However, if the control volume is a quadrilateral, one has a maximum of six secondary neighbours for the reconstruction and, therefore, 20 possibilities of stencils for selection. In Figure 1 one can see a typical neighbourhood for the implementation of the algorithm with the hatched volumes representing a possible stencil.

Although the case in which one has 20 stencils for selection can occur, in most cases, one has only five secondary neighbours for the reconstruction in quadrilaterals and, then, 10 possibilities of stencils for selection. Such a situation happens because, when selecting the stencil with the primary neighbours, one has, in most cases, a stencil that is not centred as can be viewed in

DOI: 10.1002/fld

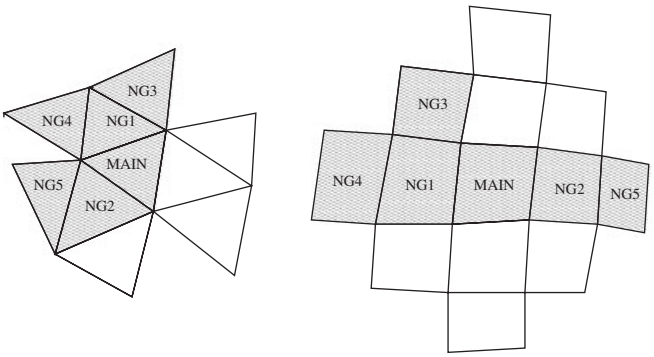

Figure 1. Typical neighbourhood for a third-order accuracy reconstruction. The hatched volumes exemplify a possible stencil for the reconstruction.

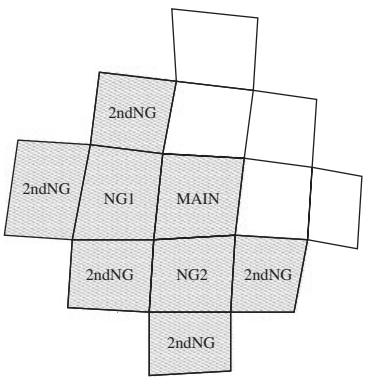

Figure 2. Non-centred neighbourhood for a third-order accuracy reconstruction in a mesh composed exclusively by quadrilaterals.

Figure 2 for the control volumes labelled NG1 and NG2. In such a case, one can see that there are five secondary neighbours (the control volumes labelled as 2nd NG). In triangular control volumes, one can have the presence of three secondary neighbours for the reconstruction, which is a bad case for reconstruction on a triangular mesh. An example of this situation can be observed in Figure 3, where the hatched control volumes NG1 and NG2 compose the smoothest stencil for a second-order reconstruction and the hatched control volumes, NG3, NG4 and NG5, are the control volumes used for the third-order reconstruction. Due to the lack of possibilities to switch the cells and, therefore, have more stencils for a third-order accuracy reconstruction, this case allows for the construction of only one stencil. If this stencil is in a discontinuous region of the flow, it will produce oscillations, and it will lead to a non-physical solution. Hence, the procedure adopted to avoid the problem where one has a stencil such this, in a discontinuous region of the flow, is to reduce the order of accuracy of the scheme in these cells.

DOI: 10.1002/fld

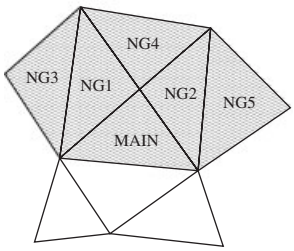

Figure 3. Bad case for a third-order reconstruction on a triangular mesh.

The algorithm here implemented has presented good results for most cases analysed in the present work. As expected, the WENO schemes presented better results with respect to the convergence ratio and with respect to the smoothness of the solution in comparison with the ENO schemes. As mentioned in the papers of Abgrall [16] and Harten and Chakravarthy [19], one has to reduce the order of accuracy in some cells to maintain the stability of the method for both ENO and WENO schemes. The technique used for the reduction of the order of accuracy is the same presented by Abgrall [16]. Such a technique computes an auxiliary term as

$$\Upsilon = \sum_{\iota=2}^{\eta} \sum_{\beta_1+\beta_2}^{\iota} |r_{\beta_1\beta_2}||(x - x_c)^{\beta_1}(y - y_c)^{\beta_2}| \tag{18}$$

and verifies if Υ is greater than the mean value of the primitive variable in the cell times a φ factor. In the affirmative case, one must reduce the order of accuracy of the scheme. The φ factor used in the present computations is $\varphi = 0.95$, as suggested in Abgrall [16]. It should be pointed out that the authors have studied several algorithms for stencil selection in Reference [1]. The algorithm which is being used in the present paper was the best compromise between computational cost and quality of the solutions.

3.3. Fourth-order implementation

For the implementation of the fourth-order accurate schemes, one must use 10 cells for the polynomial reconstructions. Nine unknown coefficients are computed for each polynomial through the solution of a 9-equation linear system. As previously discussed, the linear system matrix is composed by the control volume moments, and the primitive variables of the cells considered in the stencil form the forcing term. The algorithm implemented is again based on the ideas proposed by Abgrall [16], and it is an extension of the algorithm presented for the third-order method. Starting from the smoothest third-order stencil among the possible stencils for a quadratic reconstruction, one can initiate the procedure for the fourth-order accuracy reconstruction. One must amplify the third-order stencil adding the neighbour cells that share edges with the secondary neighbours already selected in the quadratic reconstruction. This is the cheapest algorithm to implement, in accordance with the approaches considered in Reference [1]. However, the resulting reconstruction procedure can still be considered very costly. The implemented algorithm uses this concept for both the ENO and WENO schemes for meshes composed by any type of control volume.

As an example, for a triangular control volume mesh, one can have, in the worst case, six new cells, which are the tertiary neighbours of the main control volume, for the fourth-order scheme.

DOI: 10.1002/fld

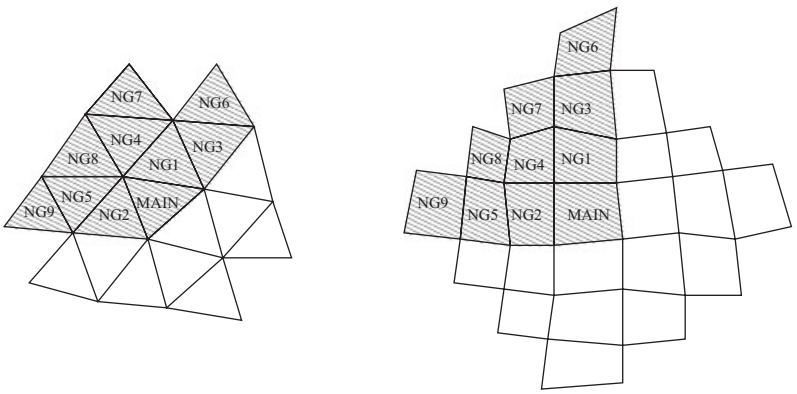

Figure 4. Typical neighbourhood for a fourth-order accuracy reconstruction. The hatched volumes exemplify a possible stencil for the reconstruction.

Such a situation provides 15 different stencils for selection. For a mesh composed by quadrilateral control volumes, the worst case leads to a reconstruction procedure that is very expensive in terms of computational cost. This worst case for a quadrilateral grid contains eight new tertiary cells for selection and, in this case, 70 different stencils could be constructed. Although the case in which one has six new cells for selection in a triangular grid, and the case in which one has eight new cells for selection in a quadrilateral grid can occur, in most cases, one has five tertiary neighbours for the reconstruction in triangles and six tertiary neighbours for the reconstruction in quadrilaterals. Then, there are five possibilities of stencils for selection in triangular grids and 15 possibilities in quadrilateral grids. In Figure 4 one can see a typical neighbourhood for the implementation of the algorithm with the hatched volumes representing a possible stencil.

4. ADAPTIVE MESH REFINEMENT

In this work, grid adaptation is used to improve the quality of the solution by increasing the number of grid points in regions where shock and expansion waves are present. Hence, a property sensor based on the solution obtained in the original mesh is computed and it is used to determine in which regions additional computational points are necessary. The general definition of the sensor, following the work in References [2, 3], can be expressed as

$$(\text{sensor})_i = \left\{ \max_m \left[\frac{|\nabla \psi_m|}{\psi_{m_{\max}} - \psi_{m_{\min}}} \right] \right\}_i \tag{19}$$

where ψ_m can be any conserved or primitive variable and $\psi_{m_{\max}}$ and $\psi_{m_{\min}}$ are the maximum and the minimum values of the ψ_m property in the flowfield. All volumes in which the sensor exceeds some specified threshold value are refined. Additional information about the implementation of the adaptive mesh refinement procedure can also be found in References [2, 3].

DOI: 10.1002/fld

5. RESULTS

The present section discusses computational results for the third- and fourth-order schemes, which are formulated for meshes composed by triangles and quadrilaterals. The objective of the present study is to verify the newly implemented capability and to assess its advantages/disadvantages with regard to the discretization methods previously available in the code [1]. Hence, the test cases here analysed are selected among those for which analytical solutions and/or well documented, independent data are available in the literature.

5.1. Ringleb flow

The first test case presents a study of the order of accuracy for the schemes analysed here using the Ringleb flow problem [20]. The Ringleb flow is basically a potential flow in a strongly bent duct and can be described analytically. At any point in the domain, the flow is characterized by two parameters, q and k. The parameter q is the non-dimensional velocity that is constant along isoline circles and the parameter k is constant along the streamlines. The domain used in the present computations has taken the streamline with $k = 0.8$ and 0.4 for the inner and outer walls of the duct, respectively. The choice of these parameters guarantees that the flow is everywhere subsonic. The inlet and the outlet of the duct are chosen as being the velocity isoline $q = 0.3$ and the boundary conditions are set in agreement with Reference [21]. An intermediate triangular mesh used in the present computations, the exact solution obtained in terms of density contours and the numerical solution obtained with the third-order WENO scheme can be observed in Figure 5. This is a steady state case and, hence, the Courant–Friedrichs–Lewy (CFL) number is set as a constant value. The CFL value used in this test case was CFL = 0.3 for both the third- and fourth-order schemes.

For this test case, the order of accuracy of the ENO and WENO schemes is measured through the computation of the $L2$ norm of the error in the density distribution as a function of the mesh refinement. The solutions are carried out with the third-order ENO and WENO schemes and the fourth-order ENO and WENO schemes using the Jiang and Shu [18] oscillation indicator. All the calculations performed for this test case considered the Roe flux difference splitting method for the numerical flux computation. The slope of the best-fit least-square line, through a plot of the

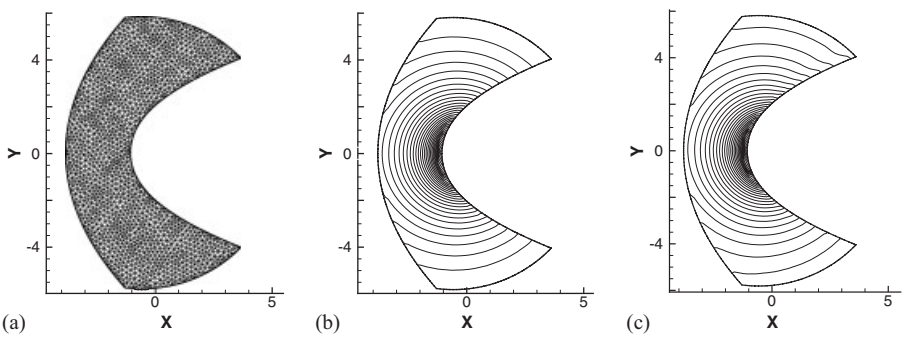

Figure 5. Computational grid and solutions for the Ringleb flow problem: (a) intermediate mesh used in the Ringleb flow computations; (b) density contour lines of the exact solution; and (c) density contour lines for the numerical solution obtained with the third-order WENO method.

DOI: 10.1002/fld

Table I. Order of accuracy for Ringleb flow computation obtained with a least-square line fit.

Method	Order of accuracy
Third-order ENO	1.96
Third-order WENO	2.66
Fourth-order ENO	1.91
Fourth-order WENO	2.16

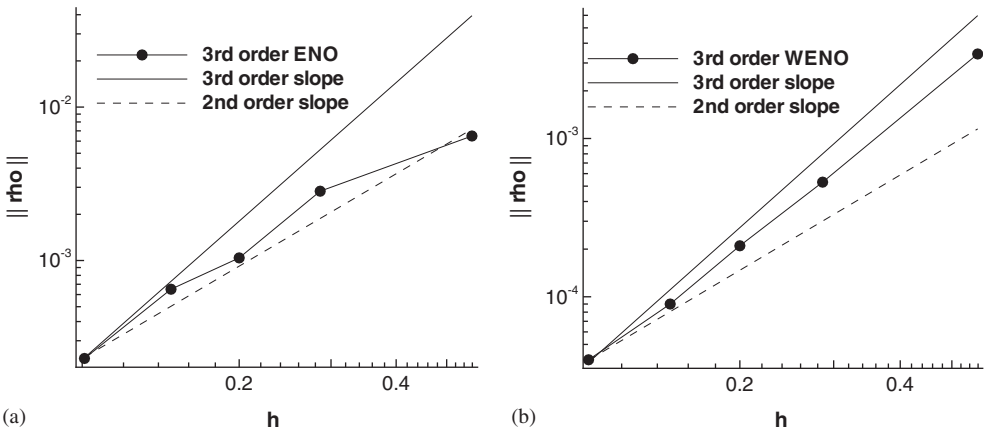

Figure 6. Discrete $L2$ norm of density error as a function of mesh size, h, in log–log plot: (a) results obtained for third-order ENO-Roe reconstruction and (b) results obtained for third-order WENO-Roe reconstruction.

logarithm of the $L2$ norm of the density error as a function of the logarithm of the mesh size gives a measure of the true order of accuracy of the method.

The results of such study are shown in Table I for all cases considered here. The third-order methods are shown in Figure 6 together with the slopes that indicate ideal second- and third-order accuracy. One can observe in Table I that the third-order ENO scheme achieved only second-order accuracy, while the third-order WENO scheme presented the best results in terms of order of accuracy. The actual order of accuracy obtained with the third-order WENO scheme is 2.66, which is only slightly lower than the theoretical one. In Figure 7, one can see the results for the fourth-order schemes, together with the slopes representative of second- and third order of accuracy. The fourth-order schemes did not achieve the expected order of accuracy. While the fourth-order ENO scheme presented almost second order of accuracy, the fourth-order WENO presented an actual order of accuracy equal to 2.16. One should observe that all the computations performed in this test case considered meshes composed exclusively by triangular control volumes.

The results for the third- and fourth-order schemes are directly related to the reconstructions close to the boundaries. In such regions, the algorithm for stencil selection does not have sufficient neighbours to reconstruct the high-order schemes and the order of accuracy decreases to second order. The results for the third-order ENO scheme are in agreement with the results shown in

DOI: 10.1002/fld

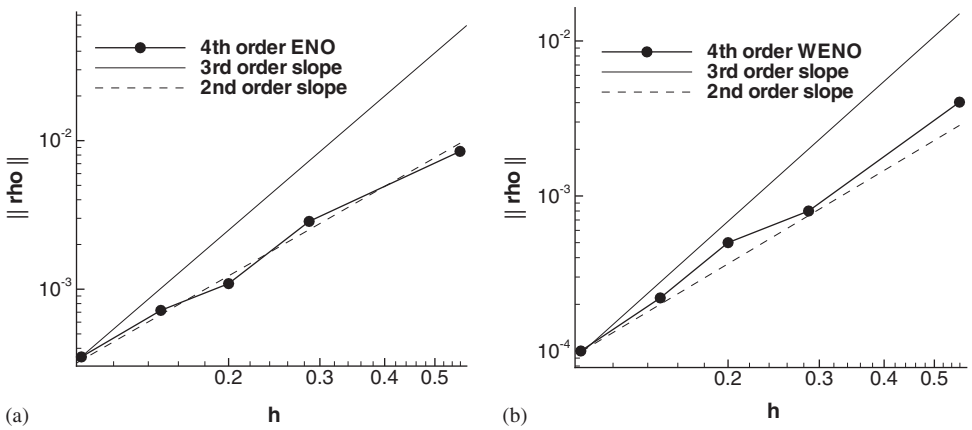

Figure 7. Discrete $L2$ norm of density error as a function of mesh size, h, in log–log plot: (a) results obtained for fourth-order ENO-Roe reconstruction and (b) results obtained for fourth-order WENO-Roe reconstruction.

Reference [13], in terms of order of accuracy. The third-order WENO scheme presented the highest value of order of accuracy, and the fourth-order schemes presented results with lower orders of accuracy than the respective third-order schemes. Again, one must emphasize that these results are strongly related to the reconstructions close to the boundary regions. Due to the lack of sufficient control volumes near the boundaries, the algorithms for stencil selection cannot find suitable stencils to maintain fourth order in such regions.

5.2. Forward-facing step

The second test case is a compressible flow in a channel with a forward-facing step that is well documented in Reference [22]. The channel length is 3, with height 1, in dimensionless units. The step is located in a position with 0.6 dimensionless units from the channel entrance. It has a height of 0.2 dimensionless units. Three different meshes are used to test the schemes. The first mesh considered in this test case has 16 384 nodes and 16 064 quadrilateral control volumes. The complete view and a blown-up view of the step region can be seen in Figure 8. The second and third meshes considered in this test case are composed exclusively by triangular control volumes and have 7022 and 13 256 nodes, and 13 608 and 25 850 control volumes, respectively. The complete view and the blown-up view of the step region for both meshes can be seen in Figure 9 for the coarse mesh, and in Figure 10, for the fine mesh. An uniform Mach number of 3.0 is set as inflow at $t = 0$ dimensionless time units. Density is made dimensionless with respect to the entrance condition and pressure is made dimensionless with respect to the entrance density times the entrance speed of sound squared. One should observe that this test case considers unsteady flow. The time step used in this test case is $\Delta t = 0.0004$ for all the schemes.

The more interesting structures of the flow develop at time equal to $t = 4.0$ dimensionless time units. Results at this instant of time appear in Figures 11–13, for the computation with WENO schemes. In Figures 11(a)–(c) one can see the solution for the second-, third- and fourth-order WENO schemes, respectively. These solutions presented in Figures 11(a)–(c) are obtained for the mesh composed exclusively by quadrilateral control volumes. In Figures 12(a) and 13(a) one can

DOI: 10.1002/fld

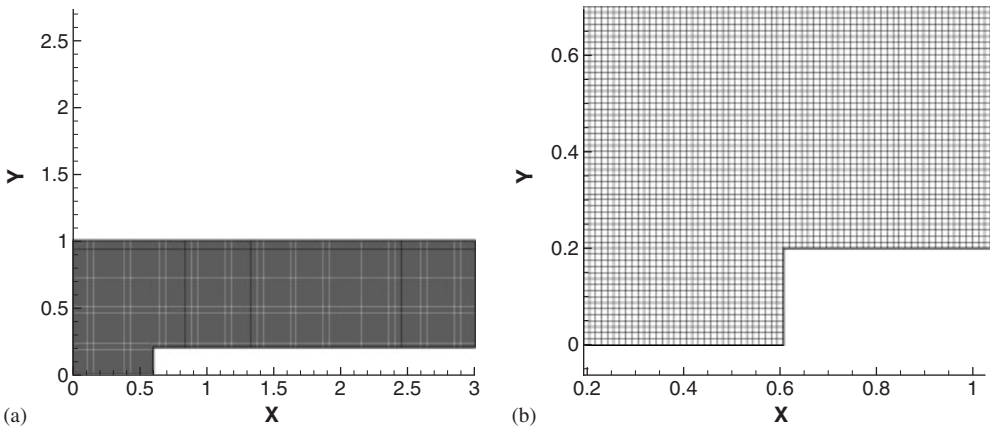

Figure 8. Mesh composed exclusively by quadrilateral control volumes used for the computation of the forward-facing step problem: (a) entire mesh for the channel and (b) detail of the mesh in the step corner region.

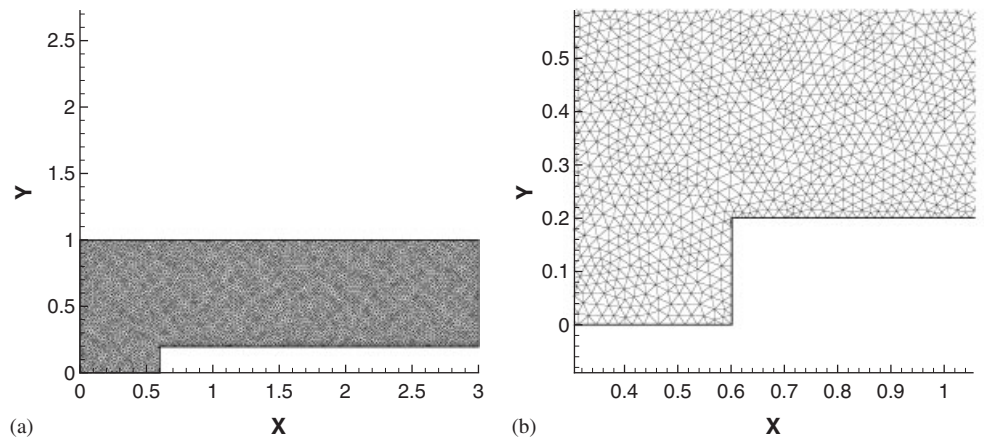

Figure 9. Coarse mesh composed exclusively by triangular control volumes used for the computation of the forward-facing step problem: (a) entire mesh for the channel and (b) detail of the mesh in the step corner region.

see the solutions for the second-order WENO scheme, in Figures 12(b) and 13(b) one can see the solutions for the third-order WENO scheme, and in Figures 12(c) and 13(c) one can see the solutions for the fourth-order WENO scheme. The solutions presented in Figure 12 are obtained for the coarse triangular mesh and the solutions in Figure 13 are obtained for the fine triangular mesh. For the fine triangular mesh, one can also observe the solution for a second-order MUSCL scheme in Figure 14. Roe's flux difference splitting method is used in all the computations performed for this test case, and the minmod limiter is used in the TVD–MUSCL solution.

DOI: 10.1002/fld

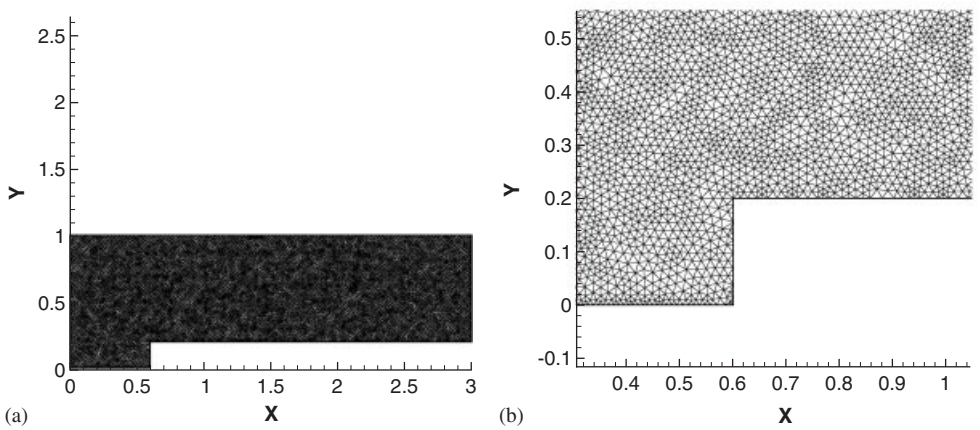

Figure 10. Fine mesh composed exclusively by triangular control volumes used for the computation of the forward-facing step problem: (a) entire mesh for the channel and (b) detail of the mesh in the step corner region.

At the instant of time presented in the solutions, a detached shock evolves to a lambda shock that reflects in the upper channel wall. A contact discontinuity is created past the lambda shock and both the reflected shock and the contact discontinuity move downstream along the channel. The reflected shock is again reflected at the lower wall as well as at the upper wall near the end of the channel. The contact discontinuity interacts with the shock that reflects in the lower wall. This interaction occurs in the region near the end of the channel, just upstream of the last shock reflection. At the corner region, there is also a weak oblique shock wave that ends the expansion region due to a Prandtl–Meyer expansion fan. This weak shock interacts with the first reflected shock near the lower wall of the channel. This typically leads to a flow structure that resembles a non-physical shock–boundary layer interaction in the region where the second shock reflection occurs. The solution in this region is very dependent on the treatment applied to the corner of the step. In the present work, no special treatment is applied to the corner of the step, contrary to the procedure adopted in the original reference [22]. One can see that the results presented here are similar to those in References [12, 16], where, as in this work, no special treatment is applied to the corner of the step.

The results obtained in Figure 11 for the mesh composed by quadrilateral control volumes present a very sharp capture of the first detached shock and of the lambda shock that reflects on the upper wall of the channel. The contact discontinuity was also well captured for the second-, third- and fourth-order WENO schemes. The first shock reflection, as well as the second reflection, were well defined in the solutions for all schemes. For the mesh in Figure 8, one can observe that the second reflection of the shock, which occurs in the lower wall, was affected by the non-physical shock–boundary layer interaction created downstream of the corner region. Such a behaviour is very pronounced for the solutions obtained with the second- and third-order WENO schemes and the quadrilateral mesh. The fourth-order WENO scheme presented a solution with a less pronounced shock–boundary layer interaction as can be seen in the Y shock formation in Figure 11(c). One can see that the WENO schemes capture the expansion fan near the corner region. However, the schemes are not able to capture the weak oblique shock created downstream

DOI: 10.1002/fld

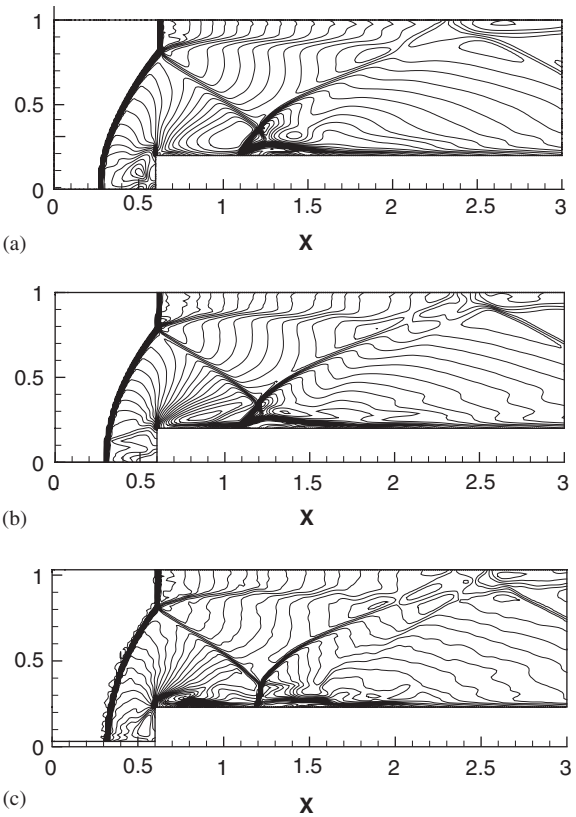

Figure 11. Mach number contours at $t = 4.0$ dimensionless time units for the mesh in Figure 8: (a) Mach number contours for the second-order WENO scheme; (b) Mach number contours for the third-order WENO scheme; and (c) Mach number contours for the fourth-order WENO scheme.

of the expansion region. Figure 11 also shows a separation bubble, in the post-shock region, in the lower wall of the channel. For the present computations, this circulation zone appears only for the calculations with the quadrilateral mesh. The region where the contact discontinuity and the second shock reflection meet and the third reflection of the shock, near the end of the channel, are better resolved by the third- and fourth-order WENO schemes.

The results in Figure 12, obtained for the coarse mesh composed by triangular control volumes, present a difference regarding the height of the lambda shock position. One can see that the lambda shock forms closer to the wall for the second-order WENO scheme and this affects the position of the contact discontinuity. In Figure 12, one can see that all the shock reflections and the contact discontinuity are better captured for the third- and fourth-order schemes. The second-order WENO scheme presents the non-physical shock–boundary layer interaction created past the corner region, in the lower wall of the channel, although such effect is much less pronounced in this case than in the solutions with the quadrilateral meshes. In other words, the second reflection of the shock presents a Y shock instead of a simple reflection at the wall. The results for the second-order scheme, in the region where the interaction between the contact discontinuity and the last shock

DOI: 10.1002/fld

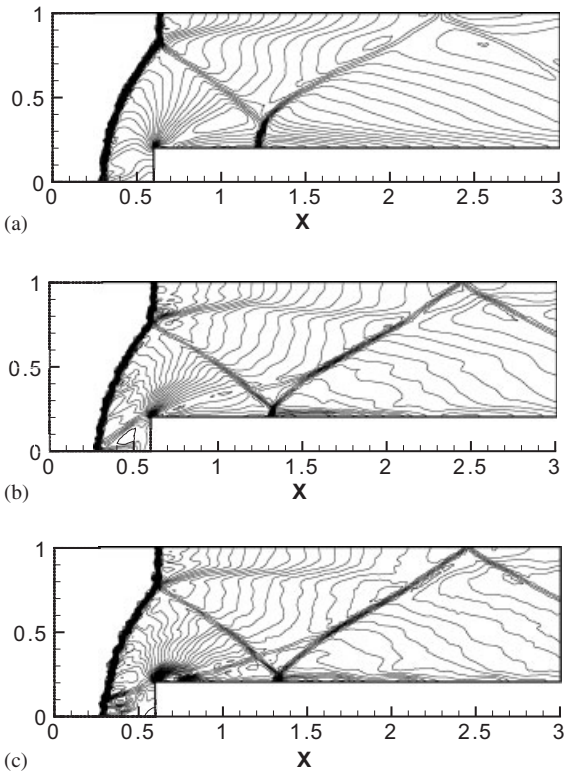

Figure 12. Mach number contours at $t = 4.0$ dimensionless time units for the mesh in Figure 9: (a) Mach number contours for the second-order WENO scheme; (b) Mach number contours for the third-order WENO scheme; and (c) Mach number contours for the fourth-order WENO scheme.

reflection occurs, are poor in comparison with the results obtained by the third- and fourth-order schemes. The third-order WENO scheme presents a poor capture of the weak shock near the corner region. However, the fourth-order scheme is the only scheme which captured it well for the triangular coarse grid. These schemes indicate a much less pronounced shock–boundary layer interaction-type phenomenon in the shock reflection along the lower wall of the channel. All shock reflections have a better resolution for the third- and fourth-order WENO schemes and they are in the correct positions, when compared to Reference [22].

The results obtained with the WENO schemes for the fine triangular mesh present the more accurate description of the flow features for this test case, as one can see in Figure 13. All the flow features are more sharply captured due to the mesh refinement. One should note that for this triangular fine grid, the Jiang and Shu [18] oscillation indicator did not present stability for the simulation with the fourth-order scheme, and, then, the oscillation indicator used in this test case, for the fourth-order scheme, was the one proposed by Harten and Chakravarthy [19]. For the second- and third-order schemes, the Jiang and Shu oscillation indicator [18] is used in the computations. For this fine mesh, the second-order WENO scheme has captured the contact discontinuity and the shock wave generated in the corner of the step differently from the results for

DOI: 10.1002/fld

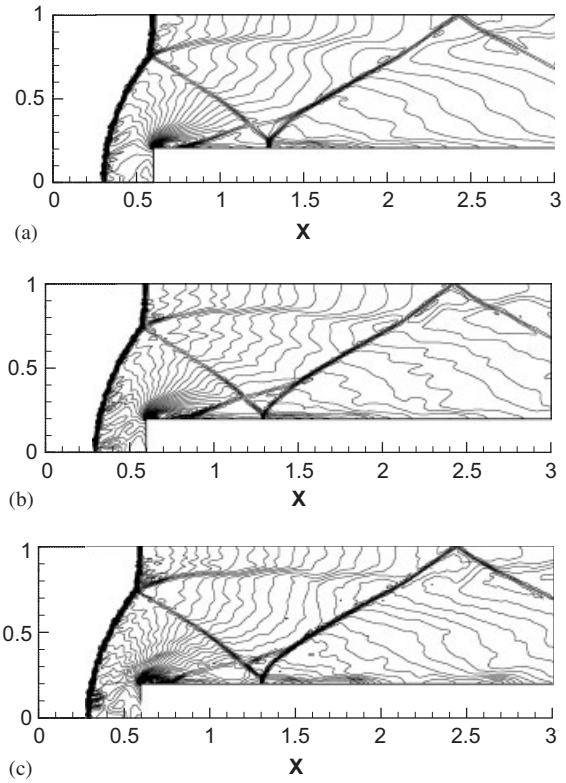

Figure 13. Mach number contours at $t = 4.0$ dimensionless time units for the mesh in Figure 10: (a) Mach number contours for the second-order WENO scheme; (b) Mach number contours for the third-order WENO scheme; and (c) Mach number contours for the fourth-order WENO scheme.

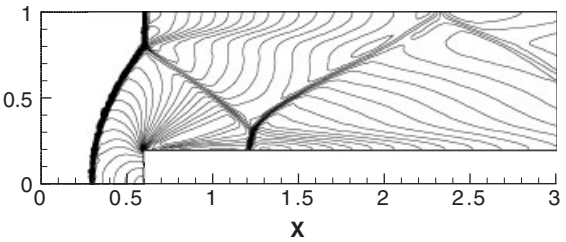

Figure 14. Mach number contours for the second-order MUSCL scheme at $t = 4.0$ dimensionless time units for the mesh in Figure 10.

the coarse triangular mesh. In Figure 14, one can observe the solution for the second-order MUSCL scheme. This scheme presents a solution much more dissipative than the solution obtained for the second-order WENO scheme. The shock reflections are poorly captured in comparison with the second-order WENO scheme, and the slip line has almost disappeared in the downstream region of the channel. This scheme does not capture the weak shock in the step corner region and, then, one

DOI: 10.1002/fld

can see the Y shock formation in the lower wall. If one compares the solution for the second-order WENO scheme, obtained for the triangular coarse mesh, with the solution for the second-order MUSCL scheme, obtained with the triangular fine mesh, one can observe the strong similarity between such solutions, at least in terms of Mach number contours.

For the third- and fourth-order scheme solutions in Figure 13, the shock wave reflections and the contact discontinuity are sharper than for the second-order scheme solution. However, as one can also observe in Figure 13, the third-order scheme presents more accurate results than the second- and the fourth-order schemes considering the resolution of the weak shock near the step corner region. One can further observe that the non-physical shock–boundary layer interaction has almost disappeared for the second- and fourth-order schemes and it has completely disappeared for the third-order scheme solution. This fact is related with the computation of the weak shock near the corner of the step. For the refined triangular mesh, the fourth-order solution is similar to the second-order one, regarding the appearance of the Y shock and the shock–boundary layer interaction. The authors believe that the better resolution of the step corner region flow obtained with the third-order scheme, compared with that obtained with the fourth-order scheme, is related to the use of the different oscillation indicators. The literature [13] presents results showing that the Jiang and Shu oscillation indicator obtains more accurate results than the Harten and Chakravarthy one. The fact the physical flow properties are better captured for this case is related to the mesh refinement and to the order of accuracy of the schemes. A refined mesh and/or a higher order scheme tend(s) to diminish the appearance of the non-physical shock–boundary layer interaction. The correct capture of the shock wave created at the corner of the step can be seen only for the triangular fine mesh, considering the second- and third-order schemes. The fourth-order scheme was able to capture the weak shock even in the coarse triangular grid. Hence, it is clear that the appearance of the non-physical shock–boundary layer interaction along the lower wall is directly related to the resolution of the corner flow, and the solution can always be improved with adequate mesh refinement. The increase in the order of accuracy of the scheme is also a determinant key ingredient to solve the problem concerning the appearance of the non-physical shock–boundary layer interaction. It is shown in the paper that, in most cases here analysed, the order of accuracy increase presents better definition for the solution. Only for the fine triangular grid, the third-order scheme presents a more accurate solution for the problem than the fourth-order one. However, as already discussed, these two solutions use different oscillation indicators and, therefore, such direct comparison is somewhat hindered.

5.3. Flow in a hypersonic inlet

The third test case discusses the computational results of the cold gas hypersonic flow in a 2-D inlet configuration which is representative of some proposed inlet geometries for typical transatmospheric vehicles. This test case is well documented in Reference [2]. For the present simulations, the fluid is treated as a perfect gas with constant specific heat and no chemistry is taken into account. The purpose of the simulations is to compare the solutions of the implemented non-oscillatory schemes in high Mach number flow conditions. Such simulations are aimed at verifying if these schemes are able to represent all flow features, such as strong shocks, shock reflections and interactions, and expansion regions. Moreover, there is interest in verifying whether the schemes can avoid oscillations in the presence of such strong discontinuities. The adaptive refinement process previously described is used in the computations, and the sensor is based on density gradients.

DOI: 10.1002/fld

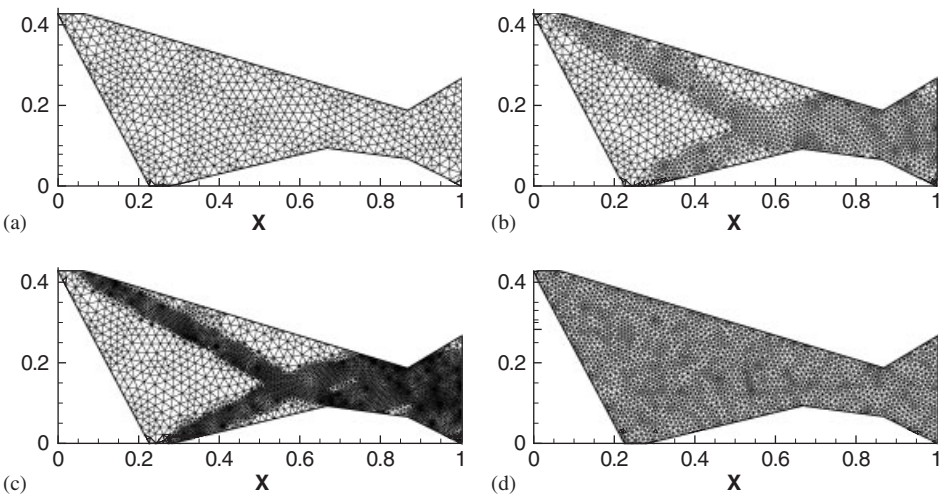

Figure 15. Complete view of the inlet meshes: (a) initial coarse mesh with 1217 volumes; (b) mesh, after one refinement pass in the initial coarse mesh, with 3091 volumes; (c) mesh, after two refinement passes in the initial coarse mesh, with 8958 volumes; and (d) initial fine mesh with 4838 volumes.

Table II. Numbers of nodes and volumes for the meshes used in the simulations of the flow in the inlet.

Mesh	Nodes	Volumes
Initial (coarse)	681	1217
After one refinement pass	1649	3091
After two refinement passes	4631	8958
Initial (fine)	2563	4838

The results considering an inlet entrance Mach number $M_e = 4$ are discussed in the present work. The simulations are performed for the initial fine mesh, without adaptive refinement, observed in Figure 15(d), and for the adaptively refined mesh, after two refinement passes, observed in Figure 15(c). The adaptively refined mesh is obtained using the flow solution computed by the third-order WENO scheme. All meshes used in the present simulations are composed exclusively by triangular control volumes. Results for quadrilateral meshes can be seen in Reference [23]. Table II indicates the characteristics of the initial and refined meshes. Moreover, in Figure 15, one can observe a complete view of the meshes. The CFL number used for all the computations in this test case is $\mathrm{CFL} = 0.2$.

The comparison among the second-, third- and fourth-order ENO and WENO scheme results is presented in Figures 16–18. One can observe in Figure 16 the results in terms of density contours for the third-order WENO scheme. The results in Figure 16(a) are obtained using the mesh in Figure 15(d), whereas those in Figure 16(b) are achieved with the mesh in Figure 15(c). Second- and fourth-order results for density contours are not presented here due to the similarity of the solutions in such overall view of the flowfield. However, the comparison among the schemes is

DOI: 10.1002/fld

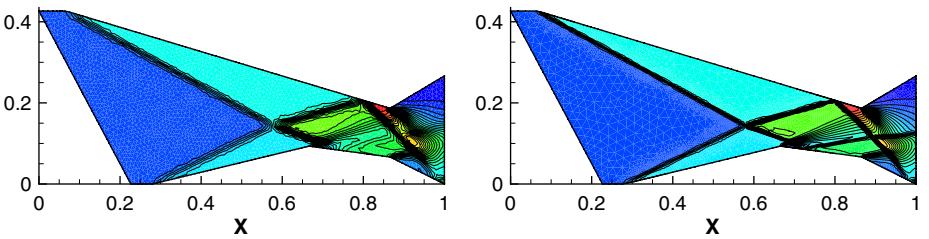

Figure 16. Inlet flow solutions for the third-order WENO scheme: (a) flow solution in terms of density contours for $M_e = 4, 0$, for the mesh in Figure 15(d) and (b) flow solution in terms of density contours for $M_e = 4, 0$, for the mesh in Figure 15(c).

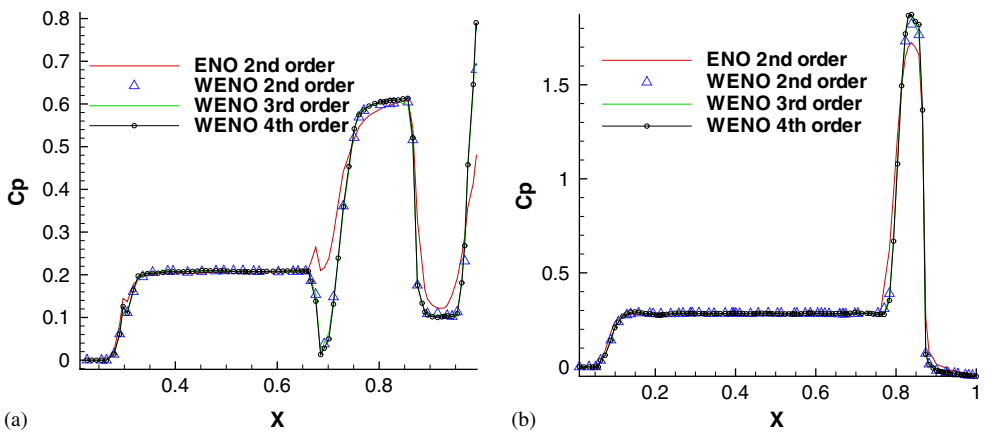

Figure 17. C_p distributions along the inlet walls for entrance Mach number $M_e = 4, 0$, obtained with the mesh of Figure 15(d): (a) C_p distribution along the lower wall and (b) C_p distribution along the upper wall.

achieved by pressure coefficient (C_p) distributions along the inlet walls. Figures 17 and 18 present the C_p distributions obtained with the various schemes.

In Figure 16, one can observe the strong oblique shocks formed along the walls of the inlet entrance. Such shock waves produce a shock–shock interaction at the dimensionless longitudinal coordinate $x = 0.58$. An expansion fan occurs in the lower wall and interacts with a shock wave resulting from the shock–shock interaction at $x = 0.66$. The shock wave which interacts with the expansion fan reflects in the lower wall of the inlet, and the other shock wave resulting from the shock–shock interaction reflects in the upper wall. Downstream of this region, one can observe an expansion fan formed in the upper wall corner and another expansion fan in the second lower wall corner. Furthermore, another shock–shock interaction occurs near the exit region of the inlet. Finally, there is a last shock reflection in the lower wall, near the exit region of the inlet.

One can observe that the physical characteristics of the flow are better defined for the simulation performed with the mesh obtained by adaptive refinement. In this test case, the two different meshes are used to verify the influence of the adaptive refinement in the solutions. The simulations

DOI: 10.1002/fld

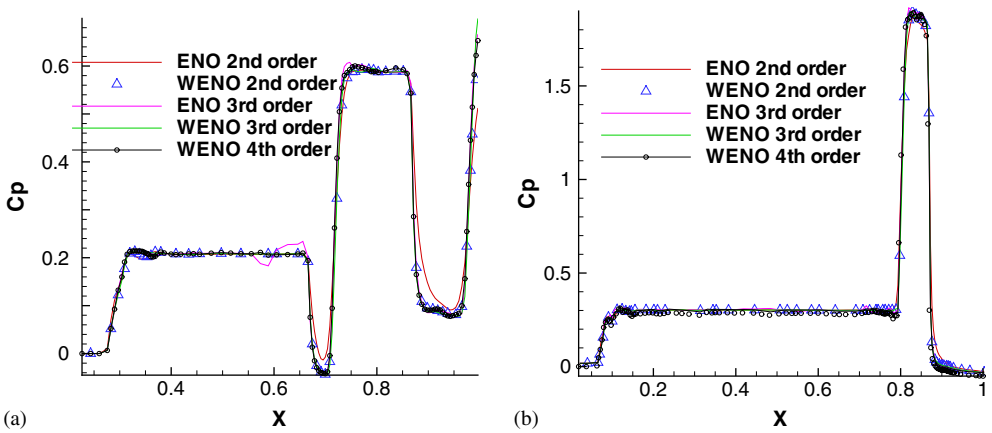

Figure 18. C_p distributions along the inlet walls for entrance Mach number $M_e = 4, 0$, obtained with the mesh of Figure 15(c): (a) C_p distribution along the lower wall and (b) C_p distribution along the upper wall.

performed in the present work have shown that higher than second-order ENO schemes are very sensitive to the meshes. The second-order ENO and WENO schemes maintain stability for both meshes used in this test. Third- and fourth-order WENO schemes present stability for both meshes, similarly to the second-order schemes. However, the third- and fourth-order ENO schemes present more sensitivity with respect to the meshes. While the third-order ENO scheme presents results only for the adaptively refined mesh, the fourth-order ENO scheme does not maintain stability with any of the inlet meshes here analysed.

Figure 17 shows the C_p distributions along the lower and upper walls of the inlet for the mesh appearing in Figure 15(d). The curves for the second-order ENO and WENO schemes and for the third- and fourth-order WENO schemes are shown. The third- and fourth-order ENO schemes have not converged for this computation. In the lower wall curve, one can clearly identify the entrance shock, which is followed by a C_p plateau, corresponding to the entrance ramp. This plateau is ended by the expansion region associated with the first kink in the lower wall. Just downstream the expansion region, there is another shock wave which increases the C_p values. Finally, one can observe the presence of an expansion fan and a last shock wave reflected in the wall. For the upper wall, one can also see the presence of the entrance shock wave, followed by a fairly long C_p plateau associated with the long entrance ramp. The C_p plateau is ended by the reflection of the shock wave, which results from the shock–shock interaction at approximately $x = 0.58$. Finally, one can note the appearance of an expansion fan, reducing the C_p values until the exit section of the inlet.

The results in Figure 17 indicate that the second-order ENO scheme does not capture correctly the first expansion region in the lower wall of the inlet. The shock wave which impinges upon the wall just downstream of the expansion region is more smeared for the solution with this scheme. Therefore, the scheme cannot resolve the expansion region and the shock wave. The downstream expansion region is also captured with a lower definition, when compared to the results of the other schemes tested. The results for the second-, third- and fourth-order WENO schemes are very similar, as far as capturing the discontinuities appearing in this flow is concerned. However, along

DOI: 10.1002/fld

the lower wall, the fourth-order WENO scheme captures the first expansion region and the second shock wave more accurately.

Figure 17 also shows that, in the upper wall, the ENO scheme presents results with lower resolution when compared to the other schemes. The more accurate results are obtained by the third- and fourth-order schemes, as one can see in the second shock wave resolution. The second-order WENO scheme does not present the same peak, after the second shock reflection, for the C_p distribution as the one achieved by the third- and fourth-order WENO schemes, as can be observed in Figure 17(b).

The results presented in Figure 18 consider the C_p distributions along the lower and upper walls for the mesh appearing in Figure 15(c). All the schemes present a small oscillation downstream the first entrance shock wave. The second-order ENO scheme presents a more smeared solution to the expansion regions in the lower inlet wall, and the third-order ENO scheme presents strong oscillations in the first expansion region and smaller oscillations immediately downstream the second shock wave. The WENO schemes present similar solutions regarding the expansion regions and the second shock wave. In the last shock reflection region, in the lower wall, near the exit section of the inlet, the third-order scheme presents the highest value for the C_p, while the second-order ENO scheme presents the lowest value.

In Figure 18, for the C_p distributions along the upper wall, the schemes present an oscillation inside the first shock wave. This fact is related to the mesh definition in the region where the shock occurs. Immediately upstream the second shock region, ending the C_p plateau, the fourth-order WENO scheme presents a small oscillation. One can observe in Figure 18(b) that the second-order ENO scheme presents the more diffusive results among the schemes studied in this test case. For all schemes tested, some oscillations can also be observed in the second C_p plateau, downstream of the second shock.

5.4. Flow over a blunt body

The last test case presented considers the cold gas hypersonic flow over a 2-D blunt body with freestream Mach number $M_\infty = 20.0$ and angle of attack $\alpha = 0°$. Again, the perfect gas hypothesis is assumed, despite the high Mach numbers appearing in the studied flow. The aim of this test is to verify the behaviour of the high-order ENO and WENO schemes with relation to the appearance of the carbuncle phenomenon [24]. The carbuncle phenomenon is characterized by the appearance of a spurious disturbance behind a detached shock wave that forms over blunt bodies. The carbuncle problem was first reported in 1988 in the work of Peery and Imlay [24]. Such a numerical problem presents a stable solution which includes a recirculation bubble situated in front of the stagnation region of the flow.

In the present test case, a mesh with 1668 nodes and 3127 control volumes is used. This mesh can be viewed in Figure 19(a). The solution for this simulation is shown in Figure 19(b) in terms of pressure contours for the third-order WENO scheme. The CFL number used in the computations for this test case is $\mathrm{CFL} = 0.2$. The results for the second- and fourth-order ENO and WENO schemes and for the third-order ENO scheme are not shown in the paper since they are very similar to the third-order WENO scheme results. The computations for this test case use the Roe flux difference splitting scheme as numerical flux function.

One can observe in the detail of the stagnation region in Figure 19(c) that the third-order WENO scheme results do not present the typical recirculation bubble characteristic of the carbuncle phenomenon. The other ENO and WENO scheme results also do not present the recirculation bubble

DOI: 10.1002/fld

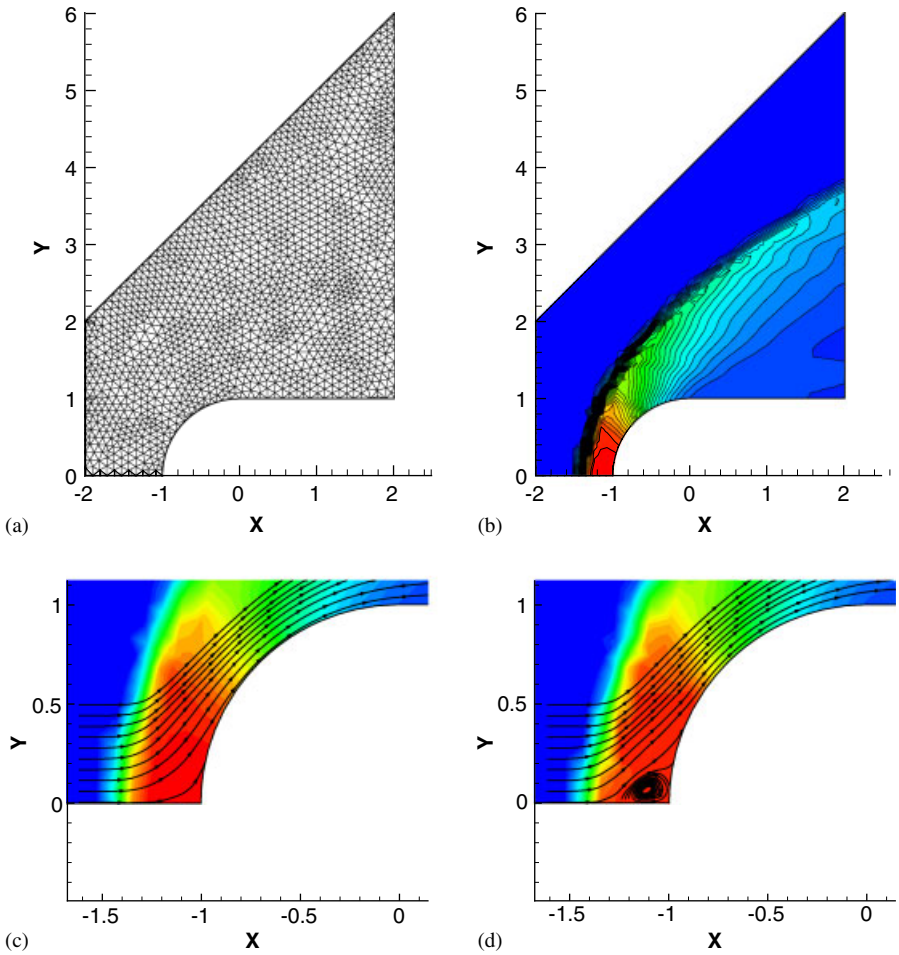

Figure 19. Pressure contours for the $M_\infty = 20.0$ flow over the 2-D blunt body: (a) mesh for the 2-D blunt body; (b) third-order WENO scheme flow solution; (c) detail of the stagnation region for the flow solution obtained with the third-order WENO scheme; and (d) detail of the stagnation region for the flow solution obtained with the TVD–MUSCL scheme.

for this simulation. In Figure 19(d), one can observe the appearance of the recirculation bubble present in the stagnation region of the blunt body for a solution obtained with the TVD–MUSCL Roe scheme for flux evaluation.

5.5. Computational cost

In this paper, algorithms for third- and fourth-order stencil selection were implemented for the ENO and WENO schemes. The results in terms of the averaged computational cost are shown in Table III. The data appearing in the table were obtained by time measurements of the simulations considering a pre-defined number of iterations. Then, all the time measurements were divided by the time of the MUSCL simulation for a mesh composed exclusively of triangular control volumes.

DOI: 10.1002/fld

Table III. Comparison of the averaged computational cost of MUSCL, ENO and WENO schemes.

Scheme	Averaged iteration cost per triangular volume	Averaged iteration cost per quadrilateral volume
MUSCL second-order	1.0	1.4
ENO second-order	1.4	2.1
WENO second-order	1.9	2.9
ENO third-order	4.7	10.5
WENO third-order	5.1	11.9
ENO fourth-order	7.6	37.8
WENO fourth-order	8.7	39.2

One can observe in Table III that the second-order ENO and WENO schemes present a computational cost between 1.4 and 2.9 times the cost of the MUSCL scheme. The higher computational cost of the non-oscillatory schemes is related to the use of the algorithms for stencil selection and, in the case of the WENO schemes, to the computation of the weights and the WENO polynomials. The third-order ENO and WENO schemes present computational costs of 3.3 and 2.7 times the costs of the respective ENO and WENO second-order schemes for a triangular mesh. One can observe, however, that the relation of these costs for a quadrilateral mesh is higher than for a triangular mesh. The costs increasing for quadrilateral meshes are directly related to the larger number of admissible stencils for third-order schemes when compared to second-order schemes in quadrilateral meshes.

As shown in Table III, the fourth-order schemes present the highest computational costs. Again, one can observe the higher costs of the schemes for quadrilateral meshes when compared to triangular meshes. Beyond the larger number of admissible stencils of the third- and fourth-order schemes, one should mention that for some test cases the order of the schemes must be reduced. The entire process of reducing the order of accuracy of the schemes is another factor that turns the computational cost higher. The authors also point out that the implementation of the ENO and WENO schemes in the code can be optimized. However, this effort is beyond the scope of the present paper.

Finally, one should mention that despite the fact that third- and fourth-order schemes present higher computational costs than second-order schemes, the higher order schemes yield solutions with a better definition of the flow features. These flow features are not captured by schemes of lower order of accuracy. For lower order schemes, it is necessary to use more refined meshes and, hence, the computational costs are higher. As one can observe, the forward-facing step case appearing in a previous section of the paper presents a comparison of solutions for schemes with different orders of accuracy using equal meshes. One can observe the sharp definition of the flow features for the third- and fourth-order schemes compared to the solutions of the second-order schemes. However, a more complete study of this type is beyond the scope of this paper.

6. CONCLUSIONS

The reconstruction of third- and fourth-order essentially non-oscillatory (ENO) schemes and weighted essentially non-oscillatory (WENO) schemes is presented in this work. Although, in

DOI: 10.1002/fld

this paper, only third- and fourth-order accurate schemes are actually implemented and assessed, the formulation of ENO and WENO reconstruction is treated in a generic framework that allows the construction of polynomials of any order and, hence, of schemes with an arbitrary order of accuracy. The flux difference splitting scheme of Roe is used as the numerical flux function in the simulations performed for this paper, and an adaptive refinement technique is employed in order to yield a sharper representation of the strong gradients appearing in the flows. The test cases studied in this work include the Ringleb flow, the supersonic flow in a channel with a forward-facing step, the flow in a typical hypersonic inlet, and the high speed flow over a 2-D blunt body.

The analysis of the effective order of accuracy of the schemes is presented for the computation of the Ringleb flow problem. The third-order WENO scheme was able to obtain an actual order of accuracy of 2.66, which is fairly close to the nominal one. The third-order ENO scheme and the fourth-order ENO and WENO schemes only reached second-order accuracy. These results are strongly related to the reconstructions close to the boundary regions.

The solutions for the quadrilateral mesh in the forward-facing step flow present a non-physical shock–boundary layer interaction with a recirculation bubble after the Y shock. The solutions for the triangular meshes show that the fourth-order WENO scheme is the only method able to capture the weak shock, in the step corner region, for the coarse triangular grid. However, for the fine triangular grid, the third-order WENO scheme captured the weak shock with a better resolution than the fourth-order scheme. The second-order WENO scheme presents a solution with much more definition for this case than the second-order MUSCL scheme.

For the flow in the hypersonic inlet, the WENO schemes have proven to be more robust than the ENO schemes. The third- and fourth-order ENO schemes have shown to be more mesh dependent for this case. One can observe that the C_p distributions along the inlet walls are very similar for the WENO schemes. The authors believe that this fact has to do with the decrease in the order of accuracy in the boundaries. Such a decrease is caused by the lack of a sufficient number of cells to reconstruct the third- and fourth-order scheme polynomials. With regard to the flow over the blunt body, one can observe that the ENO and WENO solutions do not present the carbuncle problem for the mesh and configuration used in the present work. However, for the TVD–MUSCL scheme, the carbuncle phenomenon is observed in the solution.

ACKNOWLEDGEMENTS

The authors gratefully acknowledge the support of Fundação de Amparo à Pesquisa do Estado de São Paulo (FAPESP) through a Masters Scholarship for the first author under the FAPESP Grant No. 03/10047-2. The authors also acknowledge the partial support of Conselho Nacional de Desenvolvimento Científico e Tecnológico (CNPq) under the Integrated Project Research Grant No. 501200/2003-7. The authors are also thankful to Mr Edson Basso for the very fruitful discussions during the course of the present research.

REFERENCES

1. Wolf WR, Azevedo JLF. High-order unstructured grid ENO and WENO schemes applied to aerodynamics flows. *Proceedings of the 17th AIAA Computational Fluid Dynamics Conference*, AIAA Paper No. 2005-5115, Toronto, Canada, 2005.
2. Azevedo JLF, Korzenowski H. Comparison of unstructured grid finite volume methods for cold gas hypersonic flow simulations. *Proceedings of the 16th AIAA Applied Aerodynamics Conference*, AIAA Paper No. 98-2629, Albuquerque, New Mexico, 1998.
3. Figueira da Silva LF, Azevedo JLF, Korzenowski H. Unstructured adaptive grid flow simulations of inert and reactive gas mixtures. *Journal of Computational Physics* 2000; **160**(2):522–540.

DOI: 10.1002/fld

4. Azevedo JLF, Figueira da Silva LF, Strauss D. Order of accuracy study of unstructured grid finite volume upwind schemes. *Journal of the Brazilian Society of Mechanical Sciences and Engineering* 2007, accepted for publication.
5. van Leer B. Flux–vector splitting for the Euler equations. *Proceedings of the 8th International Conference on Numerical Methods in Fluid Dynamics*. Lecture Notes in Physics, vol. 170. Springer: Berlin, 1982; 507–512.
6. Liou MS. A sequel to AUSM:AUSM+. *Journal of Computational Physics* 1996; **129**(2):364–382.
7. Roe PL. Approximate Riemann solvers, parameter vectors, and difference schemes. *Journal of Computational Physics* 1981; **43**(2):200–212.
8. Anderson WK, Thomas JL, van Leer B. A comparison of finite volume flux vector splittings for the Euler equations. *AIAA Journal* 1986; **24**(9):1453–1460.
9. Hirsch C. *Numerical Computation of Internal and External Flows*, vol. 2. Wiley: New York, 1990.
10. Harten A, Osher S, Engquist B, Chakravarthy SR. Uniformly high-order accurate essentially non-oscillatory schemes III. *Journal of Computational Physics* 1987; **71**(2):231–303.
11. Liu XD, Osher S, Chan T. Weighted essentially non-oscillatory schemes. *Journal of Computational Physics* 1994; **115**(1):200–212.
12. Sonar T. On the construction of essentially non-oscillatory finite volume approximations to hyperbolic conservation laws on general triangulations: polynomial recovery, accuracy and stencil selection. *Computer Methods in Applied Mechanics and Engineering* 1997; **140**(2):157–181.
13. Friedrich O. Weighted essentially non-oscillatory schemes for the interpolation of mean values on unstructured grids. *Journal of Computational Physics* 1998; **144**(1):194–212.
14. Shu CW, Osher S. Efficient implementation of essentially non-oscillatory shock-capturing schemes. *Journal of Computational Physics* 1988; **77**(2):439–471.
15. Gooch CFO. High order ENO schemes for unstructured meshes based on least-squares reconstruction. *Report No. P631-1296*, Argonne National Laboratory, Mathematics and Computer Science Division, 1997.
16. Abgrall R. On essentially non-oscillatory schemes on unstructured meshes: analysis and implementation. *Journal of Computational Physics* 1994; **114**(1):45–58.
17. Hu C, Shu CW. Weighted essentially non-oscillatory schemes on triangular meshes. *Journal of Computational Physics* 1999; **150**(1):97–127.
18. Jiang GS, Shu CW. Efficient implementation of weighted ENO schemes. *Journal of Computational Physics* 1996; **126**(1):77–99.
19. Harten A, Chakravarthy SR. Multi-dimensional ENO schemes for general geometries. *ICASE Report No. 91-76*, 1991.
20. Shapiro AH. *The Dynamics and Thermodynamics of Compressible Fluid Flow*, vol. 2. The Ronald Press: New York, 1954.
21. Vankeirsbilck P, Deconinck H. Higher order upwind finite volume schemes with ENO-properties for general unstructured meshes. *AGARD Report No. 787*, 1992.
22. Woodward P, Colella P. The numerical simulation of two dimensional fluid flow with strong shocks. *Journal of Computational Physics* 1984; **54**(1):115–173.
23. Wolf WR, Azevedo JLF. Essentially non-oscillatory schemes on cold gas hypersonic flow simulations. *Proceedings of the XXVI Iberian Latin–American Congress on Computational Methods in Engineering*, Guarapari, ES, Brazil, 2005.
24. Perry KM, Imlay ST. Blunt body flow simulations. *24th AIAA Joint Propulsion Conference*, AIAA Paper No. 88-2904, Boston, MA, 1988.

DOI: 10.1002/fld